Spectrochimica Acta Part A: Molecular and Biomolecular Spectroscopy 269 (2022) 120762

Contents lists available at ScienceDirect

Spectrochimica Acta Part A: Molecular and Biomolecular Spectroscopy

journal homepage: www.elsevier.com/locate/saa

Phase transition of $Mg_3(PO_4)_2$ polymorphs at high-temperature: In-situ synchrotron X-ray diffraction and Raman spectroscopic study

Xin Hu [a,b], Kuan Zhai [a,b], Muhua Jia [a,b], Yungui Liu [c], Xiang Wu [c], Wen Wen [d], Weihong Xue [a], Shuangmeng Zhai [a,*]

[a] Key Laboratory of High-temperature and High-pressure Study of the Earth's Interior, Institute of Geochemistry, Chinese Academy of Sciences, Guiyang 550081, Guizhou, China
[b] University of Chinese Academy of Sciences, Beijing 100049, China
[c] State Key Laboratory of Geological Processes and Mineral Resources, China University of Geosciences, Wuhan, Hubei 430074, China
[d] Shanghai Synchrotron Radiation Facility, Shanghai Advanced Research Institute, Chinese Academy of Sciences, Shanghai 201204, China

HIGHLIGHTS

- X-ray diffraction patterns and Raman spectra of three $Mg_3(PO_4)_2$ polymorphs were studied up to 1173 K.
- An irreversible phase transition was observed for both $Mg_3(PO_4)_2$-II and $Mg_3(PO_4)_2$-III, whereas $Mg_3(PO_4)_2$-I is stable.
- $Mg_3(PO_4)_2$-II and $Mg_3(PO_4)_2$-III transform to $Mg_3(PO_4)_2$-I at 1073 K and 1023 K, respectively.
- The thermal expansion coefficients of three $Mg_3(PO_4)_2$ polymorphs were determined.
- The temperature-dependence of Raman vibrations of three $Mg_3(PO_4)_2$ polymorphs was analyzed.

GRAPHICAL ABSTRACT

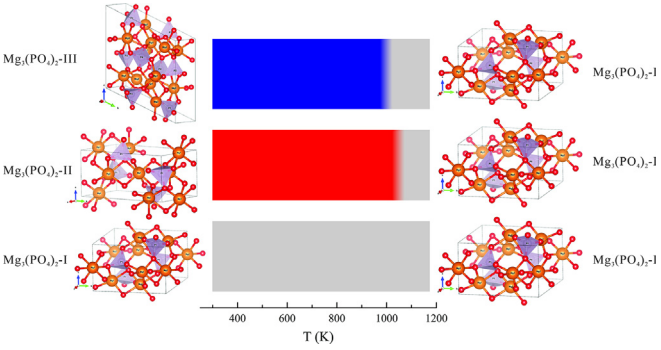

ARTICLE INFO

Article history:
Received 2 September 2021
Received in revised form 26 November 2021
Accepted 12 December 2021
Available online 16 December 2021

Keywords:
$Mg_3(PO_4)_2$ polymorphs
Phase transition
High-temperature X-ray diffraction
Raman spectroscopy
Thermal expansion
Isobaric mode Grüneisen parameters

ABSTRACT

In-situ synchrotron X-ray diffraction and Raman spectroscopy were used to study the stabilities, thermal expansion and vibrational modes of synthetic $Mg_3(PO_4)_2$. The polymorphs ($Mg_3(PO_4)_2$-I, II, III) were investigated in the temperature range of 299 ~ 1173 K at ambient pressure. An irreversible phase transition was observed for both $Mg_3(PO_4)_2$-II and $Mg_3(PO_4)_2$-III, whereas $Mg_3(PO_4)_2$-I is stable in the present study. Based on the in-situ synchrotron X-ray diffraction and Raman spectroscopic measurements, $Mg_3(PO_4)_2$-II and $Mg_3(PO_4)_2$-III transform to $Mg_3(PO_4)_2$-I at 1073 K and 1023 K, respectively. The volumetric thermal expansion coefficients of $Mg_3(PO_4)_2$-I, II and III were determined as $3.31(4) \times 10^{-5}\ K^{-1}$, $3.91(4) \times 10^{-5}\ K^{-1}$, and $3.25(5) \times 10^{-5}\ K^{-1}$, respectively. All three $Mg_3(PO_4)_2$ polymorphs show axial thermal expansive anisotropy since the thermal expansion coefficients along different axes are inconsistent. The effect of temperature on the Raman vibrations of the three $Mg_3(PO_4)_2$ polymorphs was quantitatively analyzed. And the isobaric mode Grüneisen parameters of three $Mg_3(PO_4)_2$ polymorphs are calculated, which are in the range of 0.07 ~ 3.54.

* Corresponding author.
E-mail address: zhaishuangmeng@mail.gyig.ac.cn (S. Zhai).

https://doi.org/10.1016/j.saa.2021.120762
1386-1425/

1. Introduction

The family of orthophosphate is plentiful and has been studied widely [1–15]. Magnesium orthophosphate, $Mg_3(PO_4)_2$, has been paid great attention due to its captivating structure and physiochemical properties [16–24]. There are at least three polymorphs of $Mg_3(PO_4)_2$. Farringtonite, $Mg_3(PO_4)_2$-I, is an end-member of $(Fe,Mg,Mn)_3PO_4$ solid solutions [25]. $Mg_3(PO_4)_2$ has two high-pressure phases including $Mg_3(PO_4)_2$-II (chopinite) and $Mg_3(PO_4)_2$-III [26–30].

The crystal structures of the three polymorphs were well determined in previous studies [26–27,31–32], as shown in Fig. 1. $Mg_3(PO_4)_2$-I and $Mg_3(PO_4)_2$-II belong to the $P2_1/n$ space group, where PO_4 tetrahedra of $Mg_3(PO_4)_2$-I are linked by an identical layer consisting MgO_5 polyhedra and MgO_6 polyhedra, while PO_4 of $Mg_3(PO_4)_2$-II are linked by two inequivalent layers of MgO_6 polyhedra and stacking along the *b*-axis. The crystal structure of $Mg_3(PO_4)_2$-III (space group *P-1*) consists of four inequivalent PO_4 tetrahedra linked by sharing corners and edges to distorted MgO_4, MgO_5 and MgO_6 polyhedra.

$Mg_3(PO_4)_2$-I is an appropriate host for both rare earth elements for luminescence materials and hard tissue implants [18–19,24]. Moreover, $Mg_3(PO_4)_2$-I applied as protecting cathode materials has attracted increasing attention because it could increase the cycle times and Li-storage capability of lithium batteries [33–34]. Similarly, $Mg_3(PO_4)_2$-II and $Mg_3(PO_4)_2$-III with the same chemical composition and similar structure may also have potential applications in improving lithium batteries and other fields. In a previous study [35], the phase diagram of $Mg_3(PO_4)_2$ polymorphs under high-pressure and high-temperature conditions was studied with quenched samples. Usually in the above mentioned applications, $Mg_3(PO_4)_2$-I is synthesized or treated under high temperatures. $Mg_3(PO_4)_2$-II and $Mg_3(PO_4)_2$-III with potential applications can be obtained by high-temperature and high-pressure experiments. Therefore, the stabilities and physiochemical properties of these three $Mg_3(PO_4)_2$ polymorphs at high temperatures are fundamental and important. However, there is little information about the stabilities and physiochemical properties of these three $Mg_3(PO_4)_2$ polymorphs at high temperatures.

By using in-situ synchrotron X-ray diffraction, the stabilities and thermal expansion of three $Mg_3(PO_4)_2$ polymorphs were investigated in this study over the temperature range of 306 ~ 1173 K. Additionally, the effects of temperature on the Raman active vibrations of the three $Mg_3(PO_4)_2$ polymorphs were quantitatively analyzed by high-temperature micro-Raman spectroscopy from 299 to 1173 K. The in-situ synchrotron X-ray diffraction and Raman spectroscopic results show that $Mg_3(PO_4)_2$-II changes into $Mg_3(PO_4)_2$-I at 1073 K, and $Mg_3(PO_4)_2$-III transfers into $Mg_3(PO_4)_2$-I at 1023 K. According to the obtained results, the isobaric mode Grüneisen parameters of three $Mg_3(PO_4)_2$ polymorphs were calculated.

2. Experimental

Pure $Mg_3(PO_4)_2$ polymorphs were obtained as described in our previous study [36]. By using high pure MgO and $NH_4H_2PO_4$ reagents from Alfa Aesar company, $Mg_3(PO_4)_2$-I polycrystalline powder was synthesized by a solid-state reaction at 1173 K for 72 h. $Mg_3(PO_4)_2$-II and $Mg_3(PO_4)_2$-III were obtained using synthetic $Mg_3(PO_4)_2$-I as the starting material at 1173 K-1.6 GPa for 48 h and 1323 K-2.2 GPa for 66 h, respectively. The conditions (temperature, pressure, and time) for synthesis of $Mg_3(PO_4)_2$-II and $Mg_3(PO_4)_2$-III were selected based on the high-pressure and high-temperature experimental study of the phase relations of $Mg_3(PO_4)_2$ in the temperature–pressure range 625–1150 °C and 0.66–2.25 GPa [35].

In-situ powder X-ray diffraction (XRD) patterns at various temperatures were collected at the BL14B1 beam line at Shanghai Synchrotron Radiation Facility (SSRF) [37]. The powdered samples in firmly filled capillaries with 0.3 mm diameter were illuminated by a synchrotron X-ray beam (beam size = 180 × 200 μm^2). In order to improve the data statistics, each sample was spun continuously during the high temperature in-situ XRD measurements. The temperature was monitored during the experiments using a K-type thermocouple, with an accuracy of about ± 1 K, held at the axis of the heating element near the tip of the capillaries. In-situ XRD patterns from ambient temperature to 1173 K with 100 K steps were collected on a Mythen 1 K linear detector in Debye-Sherrer mode [38]. In order to keep thermal equilibration, each temperature was held for about 5 mins before measurement. The wavelength of the X-ray beam was calibrated by using LaB_6 standard from NIST (660b). Each refinement of all the XRD patterns was carried out by using the full profile-fitting technique in EXPGUI/GSAS [39–40].

The Raman spectroscopic measurements at ambient pressure and various temperatures were carried out by using a Horiba LabRam HR Evolution Raman spectrometer equipped with an 1800 gr/mm grating. The method and procedure were similar to our previous studies [41–42]. A 532-nm pulsed YAG: Nd^{3+} laser beam with a power of 100 mW was used as an excitation source. Raman scattered light from the 1 μm^2 spot on the sample surface was collected with a 100 × objective lens. Three small polycrystalline slices cut from separate $Mg_3(PO_4)_2$-I, II and III phases were placed on the sapphire window of a micro-furnace (linkamTS-600 with a temperature stability of about ± 1 K). The maximum temperature for heating was 1173 K, and the interval for collecting spectrum was 50 K. For thermal equilibrium, each temperature was held for 5 min before collecting the

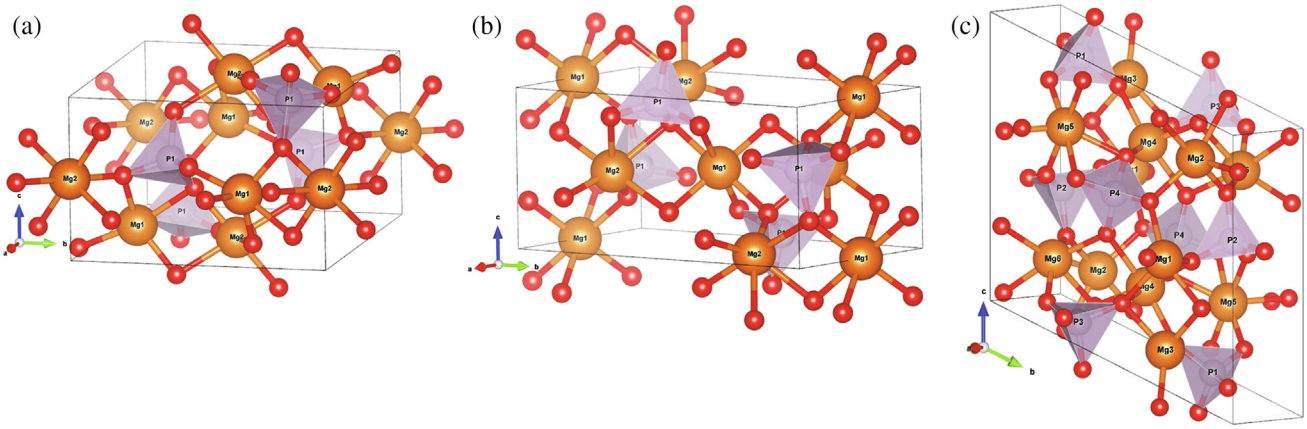

Fig. 1. The crystal structures of three $Mg_3(PO_4)_2$ polymorphs. (a) $Mg_3(PO_4)_2$-I, (b) $Mg_3(PO_4)_2$-II, and (c) $Mg_3(PO_4)_2$-III.

spectrum. The acquisition time of Raman spectra was 80 s and the spectrum ranges from 50 to 1300 cm^{-1}. Spectra were calibrated using the 520.5 cm^{-1} line of a silicon wafer. All the Raman spectra were analyzed by using the PeakFit program (SPSS Inc., Chicago) to get reasonable approximations.

3. Results and discussion

3.1. Phase transformation

The selected XRD patterns and Raman spectra of $Mg_3(PO_4)_2$ polymorphs at various temperatures and ambient pressure are shown in Fig. 2 and Fig. 3, respectively.

Based on the XRD patterns, $Mg_3(PO_4)_2$-I is stable up to 1173 K, as shown in Fig. 2(a), whereas phase transformations occur for both $Mg_3(PO_4)_2$-II and $Mg_3(PO_4)_2$-III at 1073 K, as shown in Fig. 2 (b) and (c), respectively. The phase transition of $Mg_3(PO_4)_2$-II at 1073 K was inferred from the mutations at the positions of the two most intense peaks and the obvious appearance of new peaks around 2θ of 7.00°, 9.45°, 9.68° and 11.26°. Similarly, drastic changes occur in the XRD pattern of $Mg_3(PO_4)_2$-III at 1073 K. It is noted that the increase in signal-to-noise reveals that $Mg_3(PO_4)_2$-III transforms to a higher symmetrical crystal structure. Compared to the XRD patterns in Fig. 2, it is concluded that both $Mg_3(PO_4)_2$-II and $Mg_3(PO_4)_2$-III transform into $Mg_3(PO_4)_2$-I at high temperature. After cooling to 311 K, the XRD patterns for all three samples are consistent with the initial XRD pattern of $Mg_3(PO_4)_2$-I at ambient conditions. This indicates that the temperature-induced phase transition of $Mg_3(PO_4)_2$-II and $Mg_3(PO_4)_2$-III is irreversible.

According to the Raman spectra at various temperatures, as shown in Fig. 3, $Mg_3(PO_4)_2$-I is stable though its Raman active bands become broader with increasing temperatures up to 1173 K. It is clear that $Mg_3(PO_4)_2$-II is stable up to 1023 K and transforms into $Mg_3(PO_4)_2$-I at 1073 K, as shown in Fig. 3(b). And $Mg_3(PO_4)_2$-III is stable up to 973 K though some Raman peaks merge and it transforms into $Mg_3(PO_4)_2$-I at 1023 K, as shown in Fig. 3(c). During cooling, the phase transition of $Mg_3(PO_4)_2$-II and $Mg_3(PO_4)_2$-III at high temperature is not reversible, since final

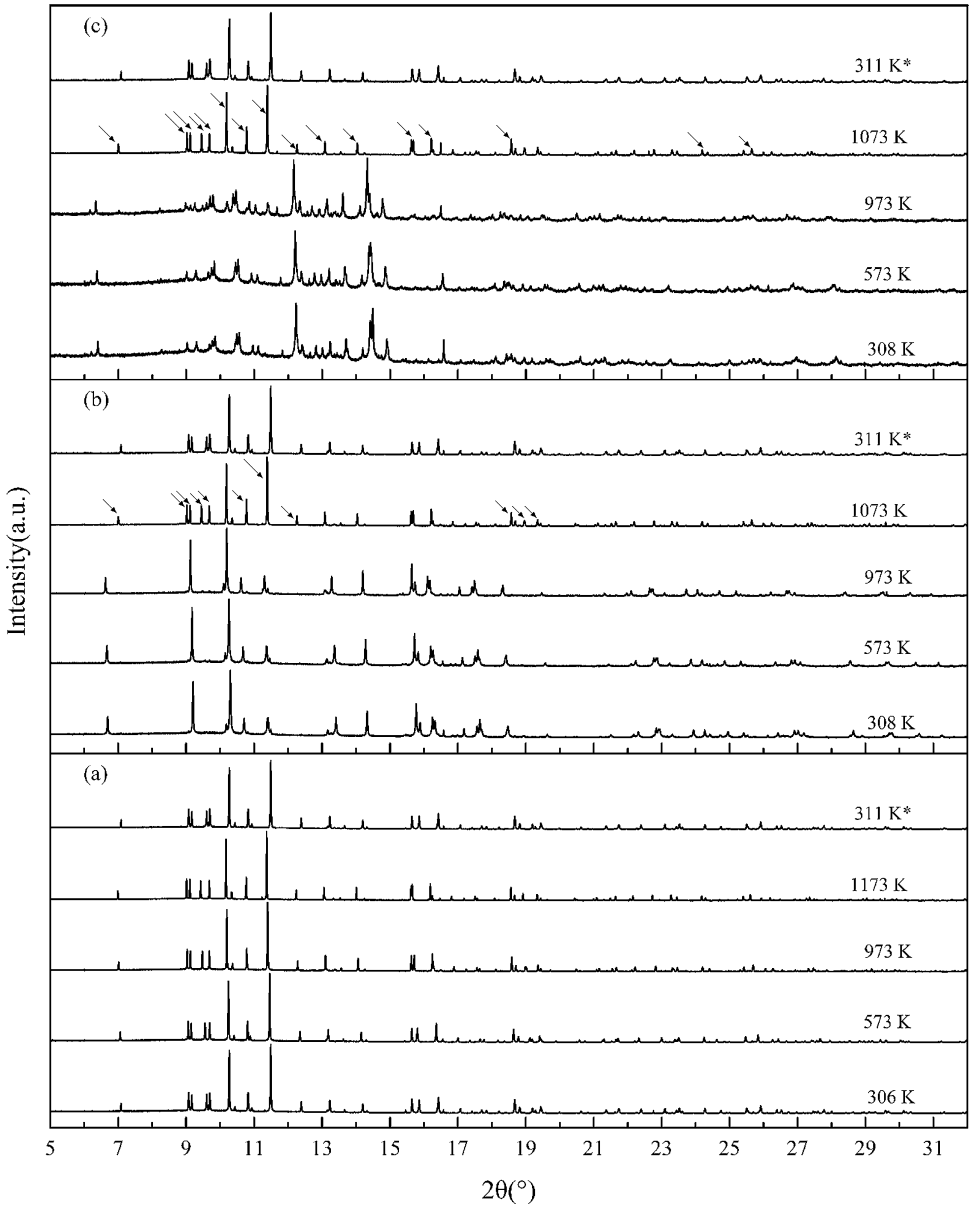

Fig. 2. The typical XRD patterns of (a) $Mg_3(PO_4)_2$-I, (b) $Mg_3(PO_4)_2$-II and (c) $Mg_3(PO_4)_2$-III up to 1173 K at ambient pressure. The temperatures with asterisk symbols represent the XRD patterns collected during cooling.

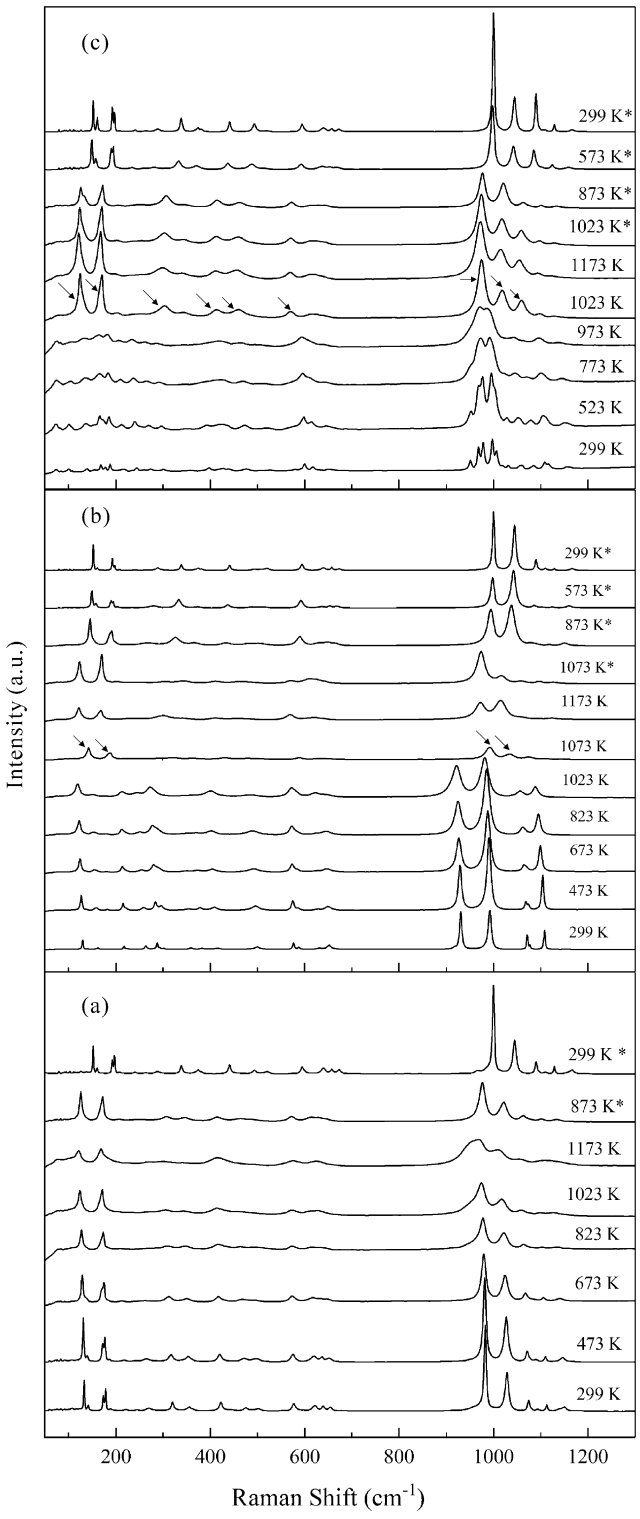

Fig. 3. The typical Raman spectra of (a) $Mg_3(PO_4)_2$-I, (b) $Mg_3(PO_4)_2$-II and (c) $Mg_3(PO_4)_2$-III up to 1173 K at ambient pressure. The tenmperatures with asterisk symbols represented the Raman spectra collected during cooling.

collected Raman spectra show the characteristics of $Mg_3(PO_4)_2$-I at ambient conditions.

The combined high-temperature in-situ XRD and Raman spectroscopic measurements, show that the temperatures for the phase transformation of $Mg_3(PO_4)_2$-II and $Mg_3(PO_4)_2$-III into $Mg_3(PO_4)_2$-I are 1073 K and 1023 K, respectively. The temperature-induced phase transitions of $Mg_3(PO_4)_2$-II and $Mg_3(PO_4)_2$-III are irreversible.

3.2. Thermal expansion

With increasing temperatures from room temperature to 1173 K, all the XRD peaks shift to the lower 2θ angle, as shown in Fig. 2. Fig. 4 illustrates typical refinements of the full X-ray diffraction patterns obtained at 473 K for the three $Mg_3(PO_4)_2$ polymorphs.

The unit-cell parameters of the three $Mg_3(PO_4)_2$ polymorphs at various temperatures were listed in Table 1. The relative variations of the unit-cell parameters (*a, b, c, V*) for the three $Mg_3(PO_4)_2$ polymorphs were plotted in Fig. 5. The obtained lattice parameters at ambient conditions are consistent with previous studies on $Mg_3(PO_4)_2$-I, II, III [25–27,31–32].

The thermal expansion coefficient $\alpha_v = 1/V\,(\partial V/\partial T)_P$ was used to describe the fluctuation of lattice parameters as a function of temperature. If the thermal expansion coefficient α_v does not vary with temperature, integration yields the following expression [43]:

$$\ln(V/V_0) = \alpha_v(T - T_0)$$

Similarly, the axial thermal expansion coefficients along *a*-, *b*- and *c*-axis can be determined by the following expressions:

$$\ln(a/a_0) = \alpha_a(T - T_0)$$

$$\ln(b/b_0) = \alpha_b(T - T_0)$$

$$\ln(c/c_0) = \alpha_c(T - T_0)$$

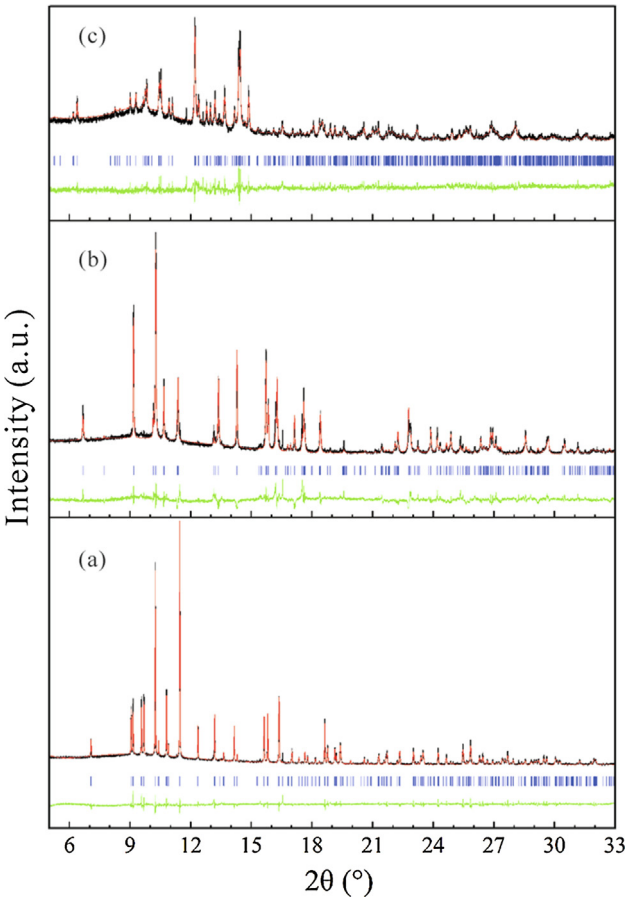

Fig. 4. Rietveld XRD patterns of $Mg_3(PO_4)_2$ polymorphs at 473 K for (a) $Mg_3(PO_4)_2$-I, (b) $Mg_3(PO_4)_2$-II and (c) $Mg_3(PO_4)_2$-III: experimental pattern (black line), calculated data (red line), positions of Bragg reflections (blue pot). The lower green curve were the difference profile.

Table 1
Lattice parameters of $Mg_3(PO_4)_2$ polymorphs at various temperatures.

T (K)	a (Å)	b (Å)	c (Å)	V (Å^3)
$Mg_3(PO_4)_2$-I				
306	7.5980(1)	8.2310(1)	5.0755(1)	316.61(1)
373	7.6024(1)	8.2408(1)	5.0760(1)	317.19(1)
473	7.6093(1)	8.2556(1)	5.0770(1)	318.10(1)
573	7.6171(1)	8.2720(1)	5.0785(1)	319.13(1)
673	7.6253(1)	8.2892(1)	5.0798(1)	320.22(1)
773	7.6338(1)	8.3070(1)	5.0814(1)	321.35(1)
873	7.6425(1)	8.3252(1)	5.0830(1)	322.51(1)
973	7.6511(1)	8.3442(1)	5.0845(1)	323.69(1)
1073	7.6598(1)	8.3638(1)	5.0857(1)	324.87(1)
1173	7.6694(1)	8.3861(2)	5.0868(1)	326.19(1)
$Mg_3(PO_4)_2$-II				
308	5.9027(1)	10.2085(2)	4.7361(1)	285.37(1)
373	5.9077(1)	10.2163(2)	4.7393(1)	286.02(1)
473	5.9154(1)	10.2289(3)	4.7443(1)	287.05(1)
573	5.9237(1)	10.2428(2)	4.7497(1)	288.17(1)
673	5.9324(1)	10.2571(2)	4.7555(1)	289.35(1)
773	5.9415(2)	10.2721(2)	4.7614(1)	290.58(1)
873	5.9507(1)	10.2868(2)	4.7674(1)	291.81(2)
973	5.9599(2)	10.3015(3)	4.7735(1)	293.06(1)
$Mg_3(PO_4)_2$-III				
308	8.5121(5)	8.9947(5)	9.3199(5)	564.26(6)
373	8.5184(4)	9.0032(4)	9.3261(4)	565.34(5)
473	8.5266(5)	9.0156(5)	9.3357(5)	566.91(6)
573	8.5359(5)	9.0299(5)	9.3469(5)	568.79(6)
673	8.5449(5)	9.0446(5)	9.3590(5)	570.71(6)
773	8.5549(6)	9.0600(5)	9.3716(6)	572.74(7)
873	8.5644(6)	9.0742(6)	9.3826(7)	574.79(8)
973	8.5754(8)	9.0931(7)	9.3992(9)	577.03(10)

Standard deviations are in parentheses.

Based on the obtained V-T data listed in Table 1, the thermal expansion coefficients for the three $Mg_3(PO_4)_2$ polymorphs were determined and listed in Table 2. It is noted that $Mg_3(PO_4)_2$-II shows the largest, i.e., $3.91(4) \times 10^{-5}$ K^{-1}, and $Mg_3(PO_4)_2$-I and $Mg_3(PO_4)_2$-III show similar thermal expansion coefficients since the difference is within 2%. The different thermal expansion coefficients indicate the divergence of MgOn polyhedral and PO_4 tetrahedral distortions in the three $Mg_3(PO_4)_2$ polymorphs during heating. Compared with the two $Ca_3(PO_4)_2$ polymorphs [44–45], as listed in Table 2, the $Mg_3(PO_4)_2$ polymorphs show comparable thermal expansion coefficients.

The fitted axial thermal expansion coefficients for the three $Mg_3(PO_4)_2$ polymorphs were also listed in Table 2. It is obvious that the axial thermal expansion coefficients of the three $Mg_3(PO_4)_2$ polymorphs are anisotropic. For $Mg_3(PO_4)_2$-I and $Mg_3(PO_4)_2$-III, the *b*-axis shows the largest axial thermal expansion. For $Mg_3(PO_4)_2$-II, its *a*-axis shows the largest axial thermal expansion. The degree of axial thermal expansive anisotropy for each sample is different, and $Mg_3(PO_4)_2$-I shows largest axial thermal expansive anisotropy. The axial thermal expansive anisotropy is related to the different atomic arrangements along different axes, which can be deduced from their crystal structures.

3.3. Temperature dependence of Raman spectra

According to the factor group analysis [46], there were 36 Raman modes for $Mg_3(PO_4)_2$-I and $Mg_3(PO_4)_2$-II based on the $P2_1/n$ space group with irreducible representation as 18 A_g + 18 B_g, and 78 Raman modes for $Mg_3(PO_4)_2$-III based on the *P-1* space group with irreducible representation as 78 A_g. However, due of the overlapping and/or low intensity of some Raman active modes, the number of observed Raman peaks is less than the predicted.

The Raman spectra of the three $Mg_3(PO_4)_2$ polymorphs at various temperature are shown in Fig. 3. The assignments of Raman modes of the three $Mg_3(PO_4)_2$ polymorphs were indexed according to our previous measured and theoretical study [36]. Obviously, the Raman vibrational modes shift to lower frequency regions and become broader during heating. This is reasonable since the bond length becomes larger with increasing temperature, implying weaker bonds, i.e., small force constants, and consequent lower vibrational frequencies according to Hooke's law. Though the intensities of Raman modes of the three $Mg_3(PO_4)_2$ polymorphs became lower during heating, most Raman peaks can be distinguished.

Fig. 3(a) shows the typical Raman spectra of $Mg_3(PO_4)_2$-I shifting towards low-wavenumber with increasing temperatures. As the temperature increases, most bands become weak and broad but there are no new peaks occurring though the intensity of the two most intense double peaks decreases and the peak shape broadens. Similarly, the ν_3 asymmetric stretching modes of P-O bonds are difficult to locate. The Raman spectrum measured at 299 K during cooling is in good agreement with the Raman spectrum measured at ambient conditions before heating, which is similar to that of XRD measurements for $Mg_3(PO_4)_2$-I. The combined Raman spectra and XRD measurements show that no phase transformations happen for $Mg_3(PO_4)_2$-I during heating.

Fig. 3(b) displays selected Raman spectra of $Mg_3(PO_4)_2$-II at various temperatures. There are discontinuous variations in the frequency and intensity of the Raman spectrum collected at 1073 K during heating. Clearly new Raman peaks appear as indexed by arrows in Fig. 3(b), which indicate a temperature-induced phase transformation. After phase transformation, the Raman spectra were also collected during cooling. Based on the Raman spectrum collected at 299 K after complete cooling, the product of temperature-induced phase transformation is $Mg_3(PO_4)_2$-I. It also reveals an irreversible phase transition from $Mg_3(PO_4)_2$-II to $Mg_3(PO_4)_2$-I around 1073 K, which is consistent with the results of high-temperature XRD measurements mentioned above.

Fig. 3(c) illustrates the representative Raman spectra of $Mg_3(PO_4)_2$-III at various temperatures. It is obvious that the Raman

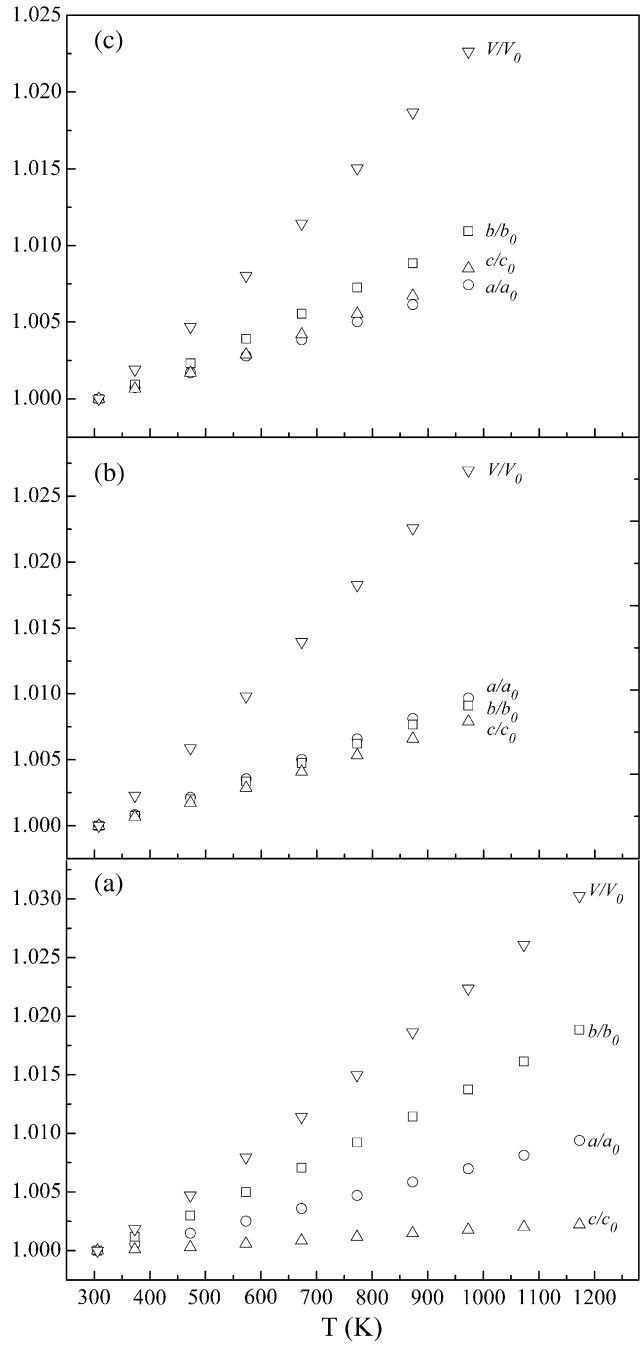

Fig. 5. Relative variations in lattice parameters and volume with temperature of (a) $Mg_3(PO_4)_2$-I, (b) $Mg_3(PO_4)_2$-II and (c) $Mg_3(PO_4)_2$-III at ambient pressure.

peaks show a red shift, become broad and merge with increasing temperature. Obviously some new Raman peaks appear at 1023 K as marked by arrows in Fig. 3(c), which indicates a temperature-induced phase transformation has happened. Compared with the XRD results, the temperature for the phase transformation is more precise, which is due to the smaller temperature interval (50 K) for Raman spectroscopic measurements than that (100 K) for XRD measurements. After phase transformation, the Raman spectra were also collected during cooling. According to the Raman spectrum collected at 299 K after complete cooling, the product of temperature-induced phase transformation is $Mg_3(PO_4)_2$-I. It also indicates an irreversible phase transition from $Mg_3(PO_4)_2$-III to $Mg_3(PO_4)_2$-I around 1023 K, which is consistent with the results of high-temperature XRD measurements mentioned above.

The variations of Raman modes at different temperatures for $Mg_3(PO_4)_2$-I are illustrated in Fig. 6(a). The constants derived by linear regressions of the vibrations are listed in Table 3. The temperature coefficients (b_i) of vibrations in $Mg_3(PO_4)_2$-I vary from $-2.24(2)$ to $-0.70(2) \times 10^{-2}$ cm^{-1} K^{-1}. The ν_3 antisymmetric stretching vibrations of $Mg_3(PO_4)_2$-I show the relatively largest temperature dependences.

The variations of Raman modes at different temperatures for $Mg_3(PO_4)_2$-II are illustrated in Fig. 6(b). The constants derived by linear regressions of the vibrations before the phase transition are listed in Table 4. The temperature coefficients (b_i) of vibrations in $Mg_3(PO_4)_2$-II vary from $-2.96(4)$ to $-0.71(4) \times 10^{-2}$ cm^{-1} K^{-1}. The Mg-O bending vibrations of $Mg_3(PO_4)_2$-II show relatively larger temperature dependences.

The variations of Raman modes at different temperatures for $Mg_3(PO_4)_2$-III are illustrated in Fig. 6(c). The constants derived by linear regressions of the vibrations before the phase transition are listed in Table 5. The temperature coefficients (b_i) of vibrations in $Mg_3(PO_4)_2$-III vary from $-4.46(2)$ to $-0.08(1) \times 10^{-2}$ cm^{-1} K^{-1}. The temperature coefficient (b_i) of $\nu_1 + \nu_3$ symmetric stretching mode at 1019 cm^{-1} of the PO_4 tetrahedra shows the largest value. It is noted that the lattice vibration of $Mg_3(PO_4)_2$-III at 73 cm^{-1} is almost independent of temperature since its temperature-dependence is close to zero (-0.08 $\times$ 10^{-2} cm^{-1} K^{-1}).

3.4. Isobaric mode Grüneisen parameters

The isobaric mode Grüneisen parameters (γ_{iP}) can be calculated by using the following expression [47–48]:

$$\gamma_{iP} = -\frac{1}{\alpha}\left(\frac{\partial ln\nu_i}{\partial T}\right)_P$$

where α is the volume thermal expansion coefficient. The obtained volume thermal expansion coefficients for the three $Mg_3(PO_4)_2$ polymorphs in this study were used, and the calculated values of γ_{iP} for different vibrational modes of the three $Mg_3(PO_4)_2$ polymorphs are also listed in Tables 3, 4, and 5, respectively.

The obtained isobaric mode Grüneisen parameters, γ_{iP}, of three $Mg_3(PO_4)_2$ polymorphs (I, II, III) are in the ranges of 0.35 ~ 2.63, 0.31 ~ 2.71, and 0.07 ~ 3.54, respectively, and their averaged isobaric mode Grüneisen parameters are 1.13, 1.16, and 1.16, respectively.

Table 2
Thermal expansion coefficients of $Mg_3(PO_4)_2$ polymorphs and comparison with other similar orthophosphates.

Formula	Space group	α_v ($\times 10^{-5}$ K^{-1})	α_a ($\times 10^{-5}$ K^{-1})	α_b ($\times 10^{-5}$ K^{-1})	α_c ($\times 10^{-5}$ K^{-1})	Reference
$Mg_3(PO_4)_2$-I	$P2_1/n$	3.31(4)	1.04(1)	2.06(3)	0.21(3)	This study
$Mg_3(PO_4)_2$-II	$P2_1/n$	3.91(4)	1.42(1)	1.34(1)	1.16(1)	This study
$Mg_3(PO_4)_2$-III	$P\text{-}1$	3.25(5)	1.09(1)	1.57(2)	1.21(2)	This study
γ-$Ca_3(PO_4)_2$	$R\text{-}3m$	3.67(3)	1.18(1)	1.18(1)	1.32(3)	[44]
β-$Ca_3(PO_4)_2$	$R3c$	3.35				[45]

Standard deviations are in parentheses.

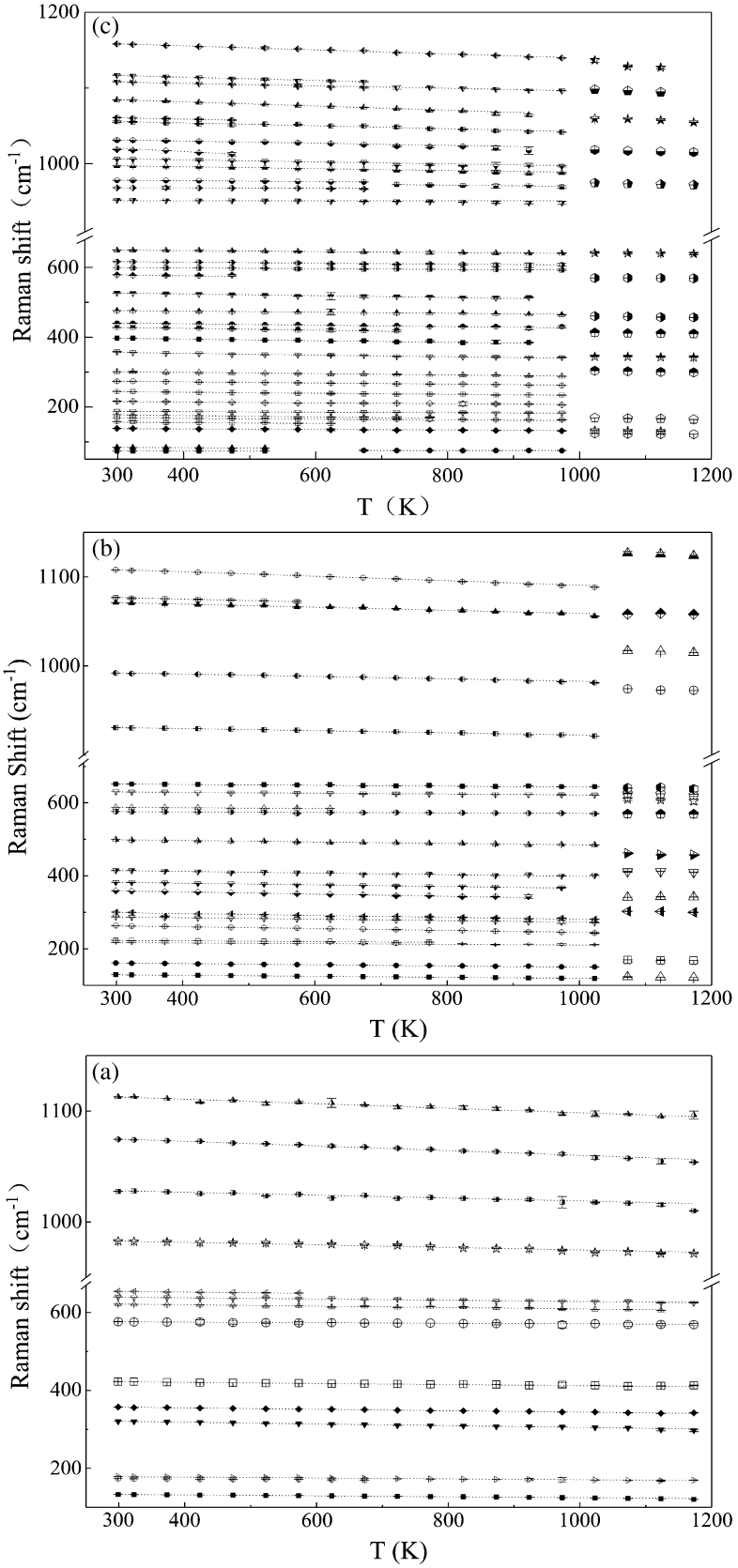

Fig. 6. Temperature dependence of the Raman modes of (a) $Mg_3(PO_4)_2$-I, (b) $Mg_3(PO_4)_2$-II and (c) $Mg_3(PO_4)_2$-III at ambient pressure.

For the PO_4 vibrational modes of $Mg_3(PO_4)_2$-I, II and III, the isobaric mode Grüneisen parameters are in the ranges of 0.35 ~ 0.84, 0.31 ~ 0.57, and 0.07 ~ 1.33, and their averaged isobaric mode Grüneisen parameters are 0.54, 0.40, and 0.51, respectively. Those

Table 3
Constants determined in $\upsilon_i = \upsilon_0 + b_i T$ of $Mg_3(PO_4)_2$-I at ambient pressure.

	υ_{i299}	υ_0	$-b_i \times 10^2$	R^2	γ_{iP}
PO_4 modes					
υ_3	1123	1118.8(3)	2.04(6)	0.985	0.55
	1075	1081.0(3)	2.09(6)	0.986	0.58
υ_1	1028	1032.1(4)	1.31(9)	0.910	0.38
	983	986.2(2)	1.13(4)	0.982	0.35
υ_4	655	660.3(2)	1.83(1)	0.969	0.84
	641	644.4(6)	1.58(10)	0.900	0.74
υ_2	577	578.3(2)	0.70(2)	0.979	0.37
Mg—O bending	422	426.6(3)	1.45(7)	0.961	1.03
	357	362.6(3)	1.82(4)	0.993	1.52
	321	327.6(2)	2.24(2)	0.998	2.07
Lattice vibration	179	182.1(2)	1.12(4)	0.970	1.86
	174	176.9(4)	1.04(9)	0.938	1.78
	131	136.5(2)	1.19(3)	0.987	2.63

υ_{i299} and υ_0 are in cm^{-1}, T in K, and the constant b_i has the corresponding units, υ_{i299} was calculated at ambient conditions, R^2 is the correlation coefficient.

Table 4
Constants determined in $\upsilon_i = \upsilon_0 + b_i T$ of $Mg_3(PO_4)_2$-II at ambient pressure.

	υ_{i299}	υ_0	$-b_i \times 10^2$	R^2	γ_{iP}
PO_4 modes					
υ_3	1108	1115.7(3)	2.49(5)	0.993	0.57
	1077	1081.9(2)	1.70(4)	0.997	0.40
	1071	1076.5(2)	1.74(3)	0.997	0.41
υ_1	992	996.3(2)	1.34(4)	0.986	0.34
	931	931.4(2)	1.19(4)	0.981	0.33
υ_4	652	655.1(3)	1.15(5)	0.973	0.45
	631	633.6(2)	1.15(4)	0.986	0.46
υ_2	587	590.1(2)	0.85(5)	0.978	0.37
	576	578.3(2)	0.71(4)	0.960	0.31
Mg—O bending	499	505.2(2)	2.01(4)	0.994	1.02
	415	421.2(9)	2.25(17)	0.921	1.37
	383	389.4(2)	2.32(5)	0.994	1.52
	359	367.8(2)	2.96(4)	0.998	2.06
	301	307.4(10)	2.64(22)	0.905	2.20
	288	293.2(2)	2.11(3)	0.996	1.84
	264	270.5(2)	2.65(6)	0.991	2.51
Lattice vibration	224	226.4(4)	1.14(9)	0.927	1.29
	217	219.9(4)	0.75(9)	0.875	0.87
	161	166.5 (1)	1.43(3)	0.995	2.20
	129	133.2 (1)	1.41(2)	0.998	2.71

υ_{i299} and υ_0 are in cm^{-1}, T in K, and the constant b_i has the corresponding units, υ_{i299} was calculated at ambient conditions, R^2 is the correlation coefficient.

averaged isobaric mode Grüneisen parameters of the PO_4 vibrational modes are comparable with those of γ-$Ca_3(PO_4)_2$ (0.58) [44] and $Ca_9NaMg(PO_4)_7$ (0.57) [49], but larger than those of $Ca_5(PO_4)_3F$ (0.30) [50] and $Sr_5(PO_4)_3F$ (0.25) [51]. The discrepancy might be related to the structural evolution of the PO_4 tetrahedra at high temperature, which is attributed to the crystal structure (arrangement of atoms) and thermal expansion. In fact, at ambient conditions, the P—O bond lengths of PO_4 tetrahedra in $Mg_3(PO_4)_2$-I is almost the same, the P—O_2 length of PO_4 tetrahedra in $Mg_3(PO_4)_2$-II is shorter than others, and the P—O bond lengths of PO_4 tetrahedra for the four unequal PO_4 tetrahedra in $Mg_3(PO_4)_2$-III are different.

For the Mg—O bending modes of $Mg_3(PO_4)_2$-I, II, and III, the isobaric mode Grüneisen parameters are in the ranges of 1.03 ~ 2.07, 1.02 ~ 2.51, and 0.98 ~ 2.06, and their averaged isobaric mode Grüneisen parameters are 1.54, 1.79, and 1.60, respectively. The scattering of γ_{iP} for the Mg-O bending modes of $Mg_3(PO_4)_2$-I is the smallest. The discrepancy of γ_{iP} for Mg-O bending modes in the three $Mg_3(PO_4)_2$ polymorphs reveals a process where the degree of distortion of the Mg-O polyhedra in $Mg_3(PO_4)_2$-I is lower than those in $Mg_3(PO_4)_2$-II and $Mg_3(PO_4)_2$-III during the thermal expansion at high temperatures.

For the lattice modes of $Mg_3(PO_4)_2$-I, II, and III, the isobaric mode Grüneisen parameters are in the ranges of 1.86 ~ 2.63, 0.87 ~ 2.71, and 0.33 ~ 3.54, and their averaged isobaric mode Grüneisen parameters are 2.09, 1.77, and 1.93, respectively. These could be explained by the more complex lattice vibrations occurring in $Mg_3(PO_4)_2$-III than those in $Mg_3(PO_4)_2$-I and $Mg_3(PO_4)_2$-II.

4. Conclusions

The crystal structure of $Mg_3(PO_4)_2$-I remains stable up to 1173 K, whereas $Mg_3(PO_4)_2$-II and $Mg_3(PO_4)_2$-III transform into $Mg_3(PO_4)_2$-I at 1073 and 1023 K, respectively, and the temperature-induced phase transition of $Mg_3(PO_4)_2$-II and $Mg_3(PO_4)_2$-III is irreversible. The thermal expansion coefficients of the three $Mg_3(PO_4)_2$ polymorphs were determined as 3.31(4) × 10^{-5} K^{-1}, 3.91(4) × 10^{-5} K^{-1}, and 3.25(5) × 10^{-5} K^{-1}, respectively. Axial thermal expansive anisotropy exists for the three $Mg_3(PO_4)_2$ polymorphs. Temperature-dependences of Raman

Table 5
Constants determined in $\upsilon_i = \upsilon_0 + b_i T$ of $Mg_3(PO_4)_2$-III at ambient pressure.

	υ_{i299}	υ_0	$-b_i \times 10^2$	R^2	γ_{iP}
PO_4 modes					
υ_3	1158	1166.3(5)	2.65(1)	0.987	0.70
	1117	1123.2(2)	2.22(1)	0.998	0.61
	1108	1112.8(3)	1.65(1)	0.985	0.46
	1085	1092.9(2)	2.78(1)	0.997	0.78
	1061	1065.4(6)	1.62(1)	0.962	0.47
	1056	1061.6(7)	1.91(1)	0.933	0.55
	1031	1035.7(4)	1.43(1)	0.961	0.42
$\upsilon_1 + \upsilon_3$	1019	1034.0(31)	4.46(2)	0.881	1.33
	1006	1010.3(3)	1.31(1)	0.945	0.40
υ_1	997	1000.8(2)	1.20(1)	0.979	0.37
	978	979.8(1)	0.56(1)	0.974	0.18
	972	979.2(12)	0.93(1)	0.862	0.29
	968	968.9(2)	0.22(1)	0.725	0.07
	952	953.4(2)	0.50(1)	0.872	0.16
υ_4	650	654.1(2)	1.39(1)	0.984	0.65
υ_2	617	620.8(3)	1.37(1)	0.961	0.68
	600	602.3(2)	0.96(1)	0.974	0.49
Mg—O bending	527	534.7(5)	2.59(2)	0.974	1.49
	476	480.9(1)	1.53(1)	0.993	0.98
	440	446.7(7)	2.01(2)	0.939	1.38
	428	436.2(5)	2.67(3)	0.976	1.88
	396	403.9(3)	2.33(3)	0.986	1.78
	358	363.5(7)	2.43(3)	0.965	2.06
Lattice vibration	301	306.5(2)	1.84(3)	0.991	1.85
	273	278.4(3)	1.61(3)	0.990	1.78
	244	248.5(2)	1.52(3)	0.990	1.88
	216	218.2(4)	1.14(2)	0.943	1.61
	188	189.5(2)	0.74(4)	0.968	1.20
	178	183.6(4)	2.11(11)	0.975	3.54
	168	171.1(2)	1.00(5)	0.961	1.80
	157	160.0(11)	1.25(13)	0.828	2.40
	139	141.1(2)	1.02(4)	0.983	2.22
	84	86.0(5)	0.72(8)	0.876	2.58
	73	73.6(4)	0.08(1)	0.901	0.33

υ_{i299} and υ_0 are in cm^{-1}, T in K, and the constant b_i has the corresponding units, υ_{i299} was calculated at ambient conditions, R^2 is the correlation coefficient.

active modes of three $Mg_3(PO_4)_2$ polymorphs were quantitatively determined and the corresponding isobaric mode Grüneisen parameters were calculated.

CRediT authorship contribution statement

Xin Hu: Investigation. **Kuan Zhai**: Data curation. **Muhua Jia**: Data curation. **Yungui Liu**: Data curation. **Xiang Wu:** Methodology, Resources. **Wen Wen:** Methodology, Resources. **Weihong Xue:** Supervision, Funding acquisition. **Shuangmeng Zhai:** Conceptualization, Supervision, Funding acquisition.

Declaration of Competing Interest

The authors declare that they have no known competing financial interests or personal relationships that could have appeared to influence the work reported in this paper.

Acknowledgements

The authors thank Dr. T. Mernagh for helpful improvement. We are grateful to two anonymous reviewers for their helpful comments and suggestion. This work was financially supported by Strategic Priority Research Program of Chinese Academy of Sciences (Grant No. XDB 41000000) and National Natural Science Foundation of China (Grant Nos: 41872045, U1932201). The in-situ synchrotron X-ray diffraction measurements were carried out at the BL14B1 beamline of the Shanghai Synchrotron Radiation Facility (Proposal No. 2020-SSRF-PT-012550).

References

[1] A.D. Toy, The Chemistry of Phosphorus: Pergamon Texts in Inorganic Chemistry, Elsevier, 1973.
[2] I.V. Tananaev, in: XXIVth International Congress of Pure and Applied Chemistry, Elsevier, 1974, pp. 75–110, https://doi.org/10.1016/B978-0-408-70578-3.50007-5.
[3] W.J. Williams, Orthophosphate, in: W.J. Williams (Ed.), Handbook of Anion Determination, Butterworth-Heinemann, 1979, pp. 445–485.
[4] N.A. Dhas, K.C. Patil, Synthesis of $AlPO_4$, $LaPO_4$ and $KTiOPO_4$ by flash combustion, J. Alloy. Compd. 202 (1993) 137–141.
[5] L. Schwarz, M. Kloss, A. Rohmann, U. Sasum, D. Haberlandl, Investigations of alkaline rare earth orthophosphates $M_3RE(PO_4)_2$, J. Alloy. Compd. 275-277 (1998) 93–95.
[6] V.A. Isupov, Phase transitions in anhydrous phosphates, vanadates and arsenates of monovalent and bivalent elements, Ferroelectrics 274 (1) (2002) 203–283.
[7] T. Znamierowska, W. Szuszkiewicz, J. Hanuza, L. Macalik, D. Hreniak, W. Stręk, Ternary orthophosphates of the $Ba_3Y_{1-x}Nd_x(PO_4)_3$ family as possible powder laser materials, J. Alloy. Compd. 341 (2002) 371–375.
[8] A.S. Wagh, Chemically Bonded Phosphate Ceramics, in: Chemically Bonded Phosphate Ceramics, Elsevier, 2004, pp. 15–27, https://doi.org/10.1016/B978-008044505-2/50006-5.
[9] A.I. Orlova, Chemistry and structural chemistry of anhydrous tri- and tetravalent actinide orthophosphates, in: S.V. Krivovichev, P.C. Burns, I.G. Tananaev (Eds.), Structural Chemistry of Inorganic Actinide Compounds, Elsevier, 2007, pp. 315–339.
[10] S.V. Dorozhkin, Biphasic, triphasic and multiphasic calcium ortho-phosphates, Acta Biomater. 8 (3) (2012) 963–977.
[11] S.V. Dorozhkin, A detailed history of calcium orthophosphates from 1770s till 1950, Mat. Sci. Eng. C 33 (2013) 3085–3110.
[12] X. Chen, Y. Dai, X. Wang, Methods and mechanism for improvement of photocatalytic activity and stability of Ag_3PO_4: A review, J. Alloy. Compd. 649 (2015) 910–932.
[13] S.V. Dorozhkin, Multiphasic calcium orthophosphate ($CaPO_4$) bioceramics and their biomedical applications, Ceram. Int. 42 (6) (2016) 6529–6554.
[14] L.V. Shvanskaya, O.S. Volkova, A.N. Vasiliev, A review on crystal structure and properties of 3d transition metal (II) orthophosphates $M_3(PO_4)_2$, J. Alloy. Compd. 835 (2020) 155028.

[15] J. Dang, D. Mei, Y. Wu, Z. Lin, A comprehensive survey on nonlinear optical phosphates: Role of multicoordinate groups, Coordin. Chem. Rev. 431 (2021) 213692.
[16] A.G. Nord, T. Stefanidis, The cation distribution between five-and six-coordinated sites in some (Mg, Me)3(PO4)2 solid solutions, Mater. Res. Bull. 15 (1980) 1183–1191.
[17] M. Sadiq, M. Bensitel, C. Lamonier, J. Leglise, Influence of the nature of precipitating basic agent on the synthesis of catalytic magnesium phosphate materials, Solid State Sci. 10 (4) (2008) 434–437.
[18] O. Kaygili, C. Tatar, F. Yakuphanoglu, Structural and dielectrical properties of Mg_3-$Ca_3(PO_4)_2$ bioceramics obtained from hydroxyapatite by sol-gel method, Ceram. Int. 38 (7) (2012) 5713–5722.
[19] Z. Zhang, W. Tang, Tunable blue-red emission and energy-transfer properties of $Mg_3(PO_4)_2$:Eu^{2+}, M^{n2}+ phosphors, Eur. J. Inorg. Chem. 2015 (23) (2015) 3940–3948.
[20] S. Debnath, S.K. Saxena, V. Nagabhatla, Facile synthesis of crystalline nanoporous $Mg_3(PO_4)_2$ and its application to aerobic oxidation of alcohols, Catal. Commun. 84 (2016) 129–133.
[21] H. Huang, J. Liu, S. Wang, Y. Jiang, D. Xiao, L.i. Ding, F. Gao, Nutrients removal from swine wastewater by struvite precipitation recycling technology with the use of $Mg_3(PO_4)_2$ as active component, Ecol. Eng. 92 (2016) 111–118.
[22] T. Brückner, K. Hurle, A. Stengele, J. Groll, U. Gbureck, Mechanical activation and cement formation of trimagnesium phosphate, J. Am. Ceramic Soc. 101 (5) (2018) 1830–1834.
[23] Y. Wang, Y. Zhou, C. Su, N.a. Tong, Z. Han, F. Liu, Effects of $Mg_3(PO_4)_2$ addition on the crystal structure, mechanical and thermophysical properties of $CaZr_4P_6O_{24}$ ceramics, J. Alloy. Compd. 806 (2019) 302–309.
[24] R. Mahajan, R. Prakash, S. Kumar, V. Kumar, R.J. Choudhary, D.M. Phase, Surface and luminescent properties of $Mg_3(PO_4)_2$: Dy^{3+} phosphors, Optik 225 (2021) 165717.
[25] E.R. DuFresne, S.K. Roy, A new phosphate mineral from the Springwater pallasite, Geochim. Cosmochim. Acta 24 (3-4) (1961) 198–205.
[26] H. Annersten, A.G. Nord, J. Songstad, K. Rundt, J. Sjöblom, T.G. Strand, V.F. Sukhoverkhov, A High-pressure phase of magnesium orthophosphate, Acta Chem. Scand. A 34a (1980) 389–390.
[27] F. Brunet, C. Chopin, A. Elfakir, M. Quarton, Crystal and powder XRD data of $Mg_3(PO_4)_2$-III: High-temperature and high-pressure form, Powder Diffract. 10 (1995) 293–295.
[28] F. Brunet, D. Vielzeuf, The farringtonite/$Mg_3(PO_4)_2$-II transformation: a new curve for pressure calibration in piston-cylinder apparatus, Eur. J. Mineral. 8 (1996) 349–354.
[29] E.S. Grew, T. Armbruster, O. Medenbach, M.G. Yates, C.J. Carson, Chopinite, $[(Mg, Fe)_3\square](PO_4)_2$, a new mineral isostructural with sarcopside, from a fluorapatite segregation in granulite-facies paragneiss, Larsemann Hills, Prydz Bay, East Antarctica, Eur. J. Mineral. 19 (2) (2007) 229–245.
[30] E.S. Grew, M.G. Yates, R.J. Beane, C. Floss, C. Gerbi, Chopinite-sarcopside solid solution, $[(Mg, Fe)_3\square](PO_4)_2$, in GRA95209, a transitional acapulcoite: Implications for phosphate genesis in meteorites, Am. Mineral. 95 (2010) 260–272.
[31] A.G. Nord, P. Kierkegaard, M. von Glehn, O. Tolboe, J. Paasivirta, The crystal structure of $Mg_3(PO_4)_2$, Acta Chem. Scand. 22 (1968) 1466–1474.
[32] S. Jaulmes, A. Elfakir, M. Quarton, F. Brunet, C. Chopin, Structure cristalline de la phase haute température et haute pression de $Mg_3(PO_4)_2$, J. Solid State Chem. 129 (2) (1997) 341–345.
[33] J. Eom, J. Cho, $Mg_3(PO_4)_2$-nanoparticle-coated $LiCoO_2$ vs $LiCo_{0.96}M_{0.04}O_2$ (M= Mg and Zn) on electrochemical and storage characteristics, J. Electrochem. Soc. 155 (2008) A201–A205.
[34] L. Xie, P. Ge, L. Zhu, X. Cao, Stabilization of LiV_3O_8 rod-like structure by protective $Mg_3(PO_4)_2$ layer for advanced lithium storage cathodes, Energy Technol. 6 (12) (2018) 2479–2487.
[35] F. Brunet, C. Chopin, F. Seifert, Phase relations in the MgO-P_2O_5-H_2O system and the stability of phosphoellenbergerite: petrological implications, Contrib. Mineral. Petr. 131 (1) (1998) 54–70.
[36] X. Hu, L. Liu, S. Zhai, The structure-Raman spectra relationships of $Mg_3(PO_4)_2$ polymorphs: A comprehensive experimental and DFT study, Spectrochim. Acta A. 245 (2021) 118906.
[37] T. Yang, W. Wen, G. Yin, X. Li, M. Gao, Y. Gu, L. Li, Y. Liu, H. Lin, X. Zhang, B. Zhao, T. Liu, Y. Yang, Z. Li, X. Zhou, X. Gao, Introduction of the X-ray diffraction beamline of SSRF, Nucl. Sci. Tech. 26 (2015) 020101.
[38] M. Gao, Y. Gu, L.i. Li, Z. Gong, X. Gao, W. Wen, Facile usage of a MYTHEN 1K with a Huber 5021 diffractometer and angular calibration in operando experiments, J. Appl. Crystallogr. 49 (4) (2016) 1182–1189.
[39] B.H. Toby, EXPGUI, a graphical user interface for GSAS, J. Appl. Crystallogr. 34 (2001) 210–213.
[40] A.C. Larson, R.B. Von Dreele, General structure analysis system (GSAS). Los Alamos Natl. Lab. Rep. LAUR, 2004 86-748.
[41] S. Zhai, K. Zhai, H. Wang, X. Wu, W. Xue, Temperature-induced phase transition of $Ca_2AlSiO_{5.5}$: Raman spectroscopic study, Vib. Spectrosc. 103 (2019) 102935.
[42] K. Zhai, W. Xue, H. Wang, X. Wu, S. Zhai, Raman spectra of sillimanite, andalusite, and kyanite at various temperatures, Phys. Chem. Miner. 47 (2020) 23.
[43] Y. Fei, Thermal Expansion, in: J.T. Ahrens (Ed.), Mineral Physics and Crystallography, American Geophysical Union, Washington D.C, 1995, pp. 29–44.
[44] S. Zhai, W. Xue, C.-C. Lin, X. Wu, E. Ito, Raman spectra and X-ray diffraction of tuite at various temperatures, Phys. Chem. Miner. 38 (8) (2011) 639–646.
[45] S. Zhai, M. Akaogi, H. Kojitani, W. Xue, E. Ito, Thermodynamic investigation on β- and γ-$Ca_3(PO_4)_2$ and the phase equilibria, Phys. Earth Planet. In. 228 (2014) 144–149.
[46] M.I. Aroyo, A. Kirov, C. Capillas, J.M. Perez-Mato, H. Wondratschek, Bilbao Crystallographic Server II Representations of crystallographic point groups and space groups, Acta Crystallogr. A 62 (2) (2006) 115–128.
[47] P. Gillet, F. Guyot, J.-M. Malezieux, High-pressure, high-temperature Raman spectroscopy of Ca_2GeO_4 (olivine form): some insights on anharmonicity, Phys. Earth Planet. In. 58 (2-3) (1989) 141–154.
[48] T. Okada, T. Narita, T. Nagai, T. Yamanaka, Comparative Raman spectroscopic study on ilmenite-type MgSiO3 (akimotoite), MgGeO3, and MgTiO3 (geikielite) at high temperatures and high pressures, Am. Mineral. 93 (1) (2008) 39–47.
[49] M. Jia, K. Zhai, M. Gao, W. Wen, Y. Liu, X. Wu, S. Zhai, X-ray diffraction and Raman spectra of merrillite at various temperatures, Vib. Spectrosc. 106 (2020) 103005.
[50] W. Xue, K. Zhai, C.-C. Lin, S. Zhai, Effect of temperature on the Raman spectra of $Ca_5(PO_4)_3F$ fluorapatite, Eur. J. Mineral. 30 (5) (2018) 951–956.
[51] W. Xue, K. Zhai, C. Lin, S. Zhai, Raman spectroscopic study on stronadelphite $Sr_5(PO_4)_3F$ at various temperatures, Vib. Spectrosc. 98 (2018) 123–127.